Thermoplastic Elastomeric Nanocomposites from Poly[styrene–(ethylene-*co*-butylene)–styrene] Triblock Copolymer and Clay: Preparation and Characterization

Anirban Ganguly, Mousumi De Sarkar, Anil K. Bhowmick

Rubber Technology Centre, Indian Institute of Technology, Kharagpur 721302, West Bengal, India

Received 3 November 2004; accepted 8 April 2005
DOI 10.1002/app.22783
Published online in Wiley InterScience (www.interscience.wiley.com).

ABSTRACT: Thermoplastic elastomer (TPE)–clay nanocomposites based on poly[styrene–(ethylene-*co*-butylene)–styrene] triblock copolymer (SEBS) were prepared. Natural sodium montmorillonite (MMT) clay was organically modified by octadecyl amine to produce an amine-modified hydrophobic nanoclay (OC). Commercially available Cloisite 20A (CL20) and Cloisite 10A, tallow ammine modified nanoclays, were also used. The intergallery spacing of MMT increased on amine modification as suggested by the shifting of the X-ray diffraction (XRD) peak from 7.6 to 4.5 and 3.8° in the cases of OC and CL20, respectively. The latter demonstrated no XRD peak when it was used at 2 and 4 parts phr in the SEBS system. Transmission electron microscopy studies showed the intercalation–exfoliation morphology in SEBS containing 4 parts of $CL20_4$–SEBS, agglomeration in SEBS having 4 parts of MMT, and mixed morphology in SEBS with 4 parts of OC systems. Locations of the clay particles were indicated by the atomic force micrographs. Mechanical and dynamic mechanical thermal analysis studies confirmed the best properties with the $CL20_4$–SEBS nanocomposites. Significant improvements in mechanical properties such as tensile strength, modulus, work to break, and elongation at break were achieved with the $CL20_4$–SEBS in polymer-layered silicate nanocomposites. Dynamic mechanical studies further showed the affinity of the organoclays toward both segments of the TPE and a compatibilization effect with CL20 at a 4-phr loading. Atomic force microscopy showed distinctly different morphologies in nanocomposites prepared through solution and melt processing. Comparisons of the mechanical, dynamic mechanical, and morphological properties of the nanocomposites prepared by melt and solution intercalation processes were done. © 2006 Wiley Periodicals, Inc. J Appl Polym Sci 100: 2040–2052, 2006

Key words: clay; elastomers; nanocomposites

INTRODUCTION

Polymer nanocomposites are recognized as one of the most promising research areas in polymer science and technology in the 21st century.[1,2] According to a report from Business Communication Co., Inc. (Norwalk, CT), the total worldwide market for polymer nanocomposites reached 11.1 million Kg, valued at US$90.8 million in 2003. This market is expected to grow at an average annual rate of 18.4% to reach US$211 million by 2008.[3]

Polymer-layered silicate nanocomposites (PLSNCs) are the foremost members of such nanocomposites. Geometrically, two-dimensional reinforcement of PLSNC is expected due to the anisotropic platelet structures of the layered silicates with higher aspect ratios.[4] The synthetic route of choice for making a nanocomposite depends on whether the final material is required in the form of an intercalated or exfoliated hybrid. The intercalation and the exfoliation mechanism of the clay particles within the polymer matrix are shown in Scheme 1. In an intercalated structure, the organic component is inserted between the layers of the clay such that the interlayer spacing is expanded but the spatial relationship to each of the layers remains unaffected. In an exfoliated morphology, the clay layers become completely separated, which renders well-distributed individual layers throughout the organic matrix (Scheme 1). In general, the interplay between entropic and enthalpic factors[5] determines whether organically modified sodium montmorillonite (MMT) clay[6,7] is dispersed, intercalated, or exfoliated in a polymer.

The field of polymer–clay nanocomposites is at a budding stage of progress today. Although it has been long known that polymers can be mixed with appropriately modified synthetic or natural clays,[8] the field of polymer–layered silicate nanocomposites has gained tremendous momentum very recently. Although they have been researched for a couple of decades only, the first commercially developed polymer nanocomposite was by the Toyota group in Ja-

Correspondence to: A. K. Bhowmick (anilkb@rtc.iitkgp.ernet.in).

Contract grant sponsor: Ministry of Human Resource Development, Government of India, New Delhi.

Contract grant sponsor: Department of Science and Technology, Government of India, New Delhi.

© 2006 Wiley Periodicals, Inc.

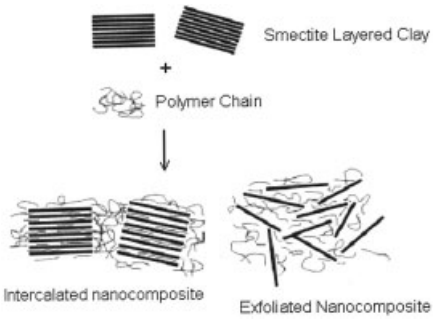

Scheme 1 Schematic representation of intercalation and exfoliation in the PLSNCs.

pan,[9] and nylon 6 was the first polymer to be used in the development of nanocomposites over a decade ago.[10] Improvements in barrier properties,[11] flame retardancy,[12] and mechanical properties have been claimed that could not have been achieved by conventional fillers at such low loadings. Development activities have spread all over the world, and active programs are now focused on the creation of nanocomposites based on nylon,[8–19] polypropylene,[20–22] polystyrene (PS),[23,24] polyethylene[25] and poly(ethylene oxide),[26] ethylene vinyl acetate,[27] and traditional thermosets.[28] The rubber nanocomposites that have been studied so far are mainly derived from unsaturated rubbers.[29–35] Rubber-based nanocomposites prepared by earlier workers from our laboratory have demonstrated interesting morphologies, which are a function of the rubber, the solvent used for casting, the nature of clay, and so on.[32–34,36] Less attention has been paid so far to the development of nanocomposites based on thermoplastics elastomers.[36,37]

In situ polymerization and solution and melt intercalation are the main synthetic routes to the formation of PLSNCs. The direct melt intercalation of a polymer into a nanoclay promises to be the most economical, environmentally friendly, polymer specific, and industrially viable process from the perspective of equivalent processing and minimum waste. However, this melt intercalation,[38,39] being environmentally benign, needs a polymer that should have good processing properties in the melting state. This technique has been successfully implemented for a few polymers to date.[37,40]

Recent advancements in PLSNCs have inspired to disperse MMT-based clay in thermoplastic elastomers (TPEs).[41] Although a few clay–styrenic block copolymer nanocomposites have been studied through melt intercalation[42,43] with compatible organophilic clays,[44] there has been almost no attempt so far to investigate clay-based nanocomposites composed of poly[styrene–(ethylene-*co*-butylene)–styrene] triblock copolymer (SEBS), except for some studies on SEBS used as a compatibilizer in solution[45,46] and in sol–gel processes.[47–49] Moreover, almost no attempt has yet been made to compare the morphology and properties of nanocomposites prepared in melt and solution intercalation processes on the same rubber.

It has to be noted that reinforcement by conventional fillers does not improve the properties of thermoplastic elastomeric block copolymer; rather, some of the properties are impaired. In addition, traditional fillers have been reported to be used at higher loadings (which increases the weight) to achieve equivalent properties.

In this study, MMT $[(Si_{7.8}Al_{0.2})^{IV}(Al_{3.4}Mg_{0.6})^{VI}O_{20}(OH)_4]$ with a net layer charge of 0.8 charges/unit cell, a smectite group of layered silicate, was chosen. For its suitable charge layer density, a 2:1 tetrahedral–octahedral layer structure, and a high aspect ratio, improvements in the polymer properties observed in earlier studies with this kind of clay included high mechanical, barrier, and thermal properties. Lamina (~1 nm thick) was separated by cations that counterbalanced the excess negative charges generated by the isomorphous substitution of atoms forming the crystal (Fig. 1).

The cation-exchange capacity (CEC) of MMT is very high because of its extensive surface area for the adsorption of water and ions. Cations, such as ammonium ion, bearing long aliphatic hydrocarbon chains compatibilize with the silicate and enhance the interaction with a polymer by enlarging (intercalate) the interlayers (lamina) and generating organically modified layered silicates, or simply, organoclays.

In this study, SEBS was used as the polymer matrix. The schematic structure of SEBS typically has a 100% triblock structure (Fig. 2), where hard PS blocks are at both ends of a saturated rubber midblock and form a body-centered cubic lattice at ambient temperature. MMT, which was organically modified by a cation-exchange reaction with a tertiary amine to give a octadecyl amine modified montmorillonite (OC), was used in this study. In addition, two types of commercially available nanoclay, Cloisite 20A (CL20) and

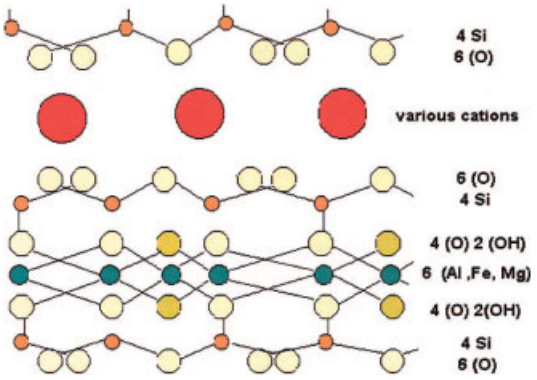

Figure 1 Diagrammatic representation of layered structure of MMT. Source: http://southwest.library.arizona.edu/azso. [Color figure can be viewed in the online issue, which is available at www.interscience.wiley.com.]

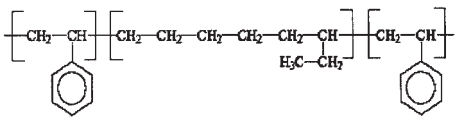

Figure 2 Schematic representation of the structure of SEBS.

Cloisite 10A (CL10), were dispersed in SEBS through both solution and melt mixing techniques. Structure–property relationships of the resultant PLSNCs were evaluated by X-ray diffraction (XRD), Fourier transform infrared spectroscopy (FTIR) studies, mechanical and dynamic mechanical property analysis, and morphological studies by transmission electron microscopy (TEM) and atomic force microscopy (AFM). This was the first detailed approach to differentiate the morphology–property relationship of block copolymeric nanocomposites through AFM studies.[47–49]

EXPERIMENTAL

Materials

SEBS (Kraton G 1652; styrene content = 30%, weight-average molecular weight = 87,000, specific gravity = 0.91 g/cc, melt index = 5 g/10 min at 230°C and with a 5-kg load) was supplied by Shell Chemical Co., Ltd. The layered silicates used for nanocomposite preparation were MMT (CEC = 92. 6 mequiv/100 g of clay) and the quaternary ammonium chloride modified clays CL10 and CL20, which were generously supplied by Southern Clay Products (Gonzales, Texas). Their characteristics are given in Table I. Octadecyl amine ($C_{18}H_{37}NH_2$), the clay modifier for MMT, was procured from Sigma Chemical Co. (St. Louis, MO). Toluene (analytical grade) was obtained from Nice Chemicals Pvt., Ltd. (Cochin, India). Ethyl alcohol was supplied by Bengal Chemicals and Pharmaceuticals (Kolkata, India). The deionized water was prepared in the laboratory.

Methodology

Preparation of nanoclay

The unmodified MMT clay was modified with octadecyl amine (a primary amine) through a cation-exchange reaction. The clay (0.5 g) was dispersed in 400 cc of water and stirred thoroughly for 30 min at 80°C. The octadecyl amine was melted at 50°C and mixed with concentrated HCl (5 cc). The mixture was stirred for 5 min with the addition of 200 cc of water. It was then carefully mixed with the aqueous clay dispersion with constant stirring for 2 h at 30°C to obtain the modified nanoclay. It was then filtered and washed thoroughly with hot water until it was free from chloride ions. The moist clay was then vacuum-dried at 30°C for 2 days.

Preparation of the SEBS–clay nanocomposites

Melt process. In the melt process, unmodified MMT and modified clays (CL10 and CL20) were mixed with SEBS in a CSI MAX mixing extruder (model CSI-194, S/N-296 by Custom Scientific Instruments, Inc., Cedar Knolls, NJ). The rotor temperature was kept at 205°C, and that of the header was kept at 210°C. The extrudate was obtained at the aforesaid temperature with the constant addition of nanoclay to keep the output fixed at 5 g/10 min. The extrudate was palletized and reextruded under identical conditions for proper dispersion of the nanoclay. Finally, the pelletized extrudates were compression-molded into a sheet about 0.5 mm thick at 210°C for 3 min in a Moore hydraulic press (George E. Moore & Son Ltd., Birmingham, UK) at a pressure of 5 MPa and were subsequently cooled down to room temperature with the pressure maintained. The details of the clay used and the composite designation are reported in Table II.

Solution process. The modified clays (OC, CL10, and CL20) were mixed with SEBS in the solution phase. Finely powdered clay, dispersed in a minimum quantity of ethanol, was added to SEBS and dissolved in toluene under constant stirring at room temperature (30°C).The resultant solution was stirred for 2 h. The amount of ethanol used to disperse the clay was very crucial because beyond a certain limit (2% with respect to toluene), it acted as a nonsolvent for SEBS. The resultant nanocomposite in solution was then allowed to stand to observe any precipitation of the clay. Thereafter, the thin film of composite was cast on a

TABLE I
Sources and Characteristics of Unmodified and Modified MMT clays

Symbol (trade name)	Organic modifier	CEC[1] or modifier concentration[2]	Weight loss on ignition (%)	Specific gravity (gm/cc)[a]	Anion
Na^+ MMT (Cloisite Na^+)	None	92.6 mequiv/100 g of clay[1]	7	2.86	None
CL20 (Cloisite 20A)	2M2HT	95 mequiv/100 g of clay[2]	38	1.77	Chloride
CL10 (Cloisite 10A)	2MBHT	125 mequiv/100 g of clay[2]	39	1.90	Chloride

2M2HT = dimethyl dihydrogenated tallow (≈65% C18, ≈30% C16, and ≈5% C14) quarternary ammonium; 2MBHT = dimethyl benzyl hydrogenated tallow (≈65% C18, ≈30%C16, and ≈5% C14) quarternary ammonium. Data provided by Southern Clay Products.

[a] ASTM D 792.

TABLE II
Designations Used for Clay and Clay–SEBS Composites

Sample	Designation
Poly[styrene–(ethylene-*co*-butylene)–styrene]copolymer	SEBS
Sodium montmorillonite clay	MMT
Polymer-layered silicate nanocomposite	PLSNC
Octadecyl amine modified montmorillonite clay	OC
Tertiary amine (with long-chain hydrogenated tallow)-modified montmorillonite clay: Cloisite 10A	CL10
Tertiary amine (with long-chain aliphatic hydrogenated tallow) modified montmorillonite clay: Cloisite 20A	CL20
SEBS cast in solution process	$SEBS_s$
SEBS molded after extrusion	$SEBS_m$
4 phr MMT in SEBS	MMT_4–SEBS
0 phr CL20 in $SEBS_s$	$CL20_0$–$SEBS_s$
2 phr CL20 in $SEBS_s$	$CL20_2$–$SEBS_s$
4 phr CL20 in $SEBS_s$	$CL20_4$–$SEBS_s$
8 phr CL20 in $SEBS_s$	$CL20_8$–$SEBS_s$
2 phr CL10 in $SEBS_s$	$CL10_2$–$SEBS_s$
4 phr CL10 in $SEBS_s$	$CL10_4$–$SEBS_s$
8 phr CL10 in $SEBS_s$	$CL10_8$–$SEBS_s$
2 phr CL20 in $SEBS_m$	$CL20_2$–$SEBS_m$
4 phr CL20 in $SEBS_m$	$CL20_4$–$SEBS_m$
8 phr CL20 in $SEBS_m$	$CL20_8$–$SEBS_m$
4 phr OC in $SEBS_s$	OC_4–$SEBS_s$
2 phr CL20 in $SEBS_s$ or in $SEBS_m$	$CL20_2$–SEBS
4 phr CL20 in $SEBS_s$ or in $SEBS_m$	$CL20_4$–SEBS
8 phr CL20 in $SEBS_s$ or in $SEBS_m$	$CL20_8$–SEBS
4 phr CL10 in $SEBS_s$ or in $SEBS_m$	$CL10_4$–SEBS

Teflon-coated mold. The composition of the composites prepared with the solution technique and their designations are reported in Table II.

Characterization of the SEBS–clay nanocomposites:

XRD studies

XRD analysis of the organically modified and the unmodified clays and the SEBS–clay nanocomposites was carried out in a Rigaku Miniflex CN 2005 X-ray diffractometer (30 kV, 10 mA; Rigaku Corporation, Tokyo, Japan) at room temperature equipped with Cu Kα radiation. The scanning rate was 2°/min (1000 cycles/s) with a goniometer angle (2θ) range of 3–10°. Subsequently, the *d*-spacing of the clay layers was calculated with Bragg's equation:

$$n\lambda = 2d\sin\,\theta \quad (1)$$

where n is the order of Bragg's diffraction (taken as 1 in the present study), λ is the wavelength of the X-ray (for the Cu target used here, $\lambda = 0.154$ nm), d is the interplanar distance, and θ is the angle of the incident radiation. The samples were placed vertically in front of the X-ray source and perpendicular to the goniometer where the goniometer was fixed, whereas the sample was rotating on the sample holder, which moved to and fro for full access of the surface and bulk to the incident X-ray.

FTIR spectroscopy studies

The IR spectra of the clays and the SEBS–clay nanocomposites were recorded with an FTIR instrument (Nicolet Nexus model, Nicolet Instrument Corporation, Madison, WI) in diffuse reflectance infrared Fourier transform (DRIFT) and in attenuated total reflectance (ATR) modes, respectively, with a 45° KRS 5 prism at room temperature. The samples were scanned within the range 4000–660 cm^{-1} with a resolution of 4 cm^{-1}. In the case of the DRIFT mode, about 1% of the clay was mixed with ultrapure KBr and was taken in DRIFT pan. The average of 32 scans for ATR mode and those of 100 scans for DRIFT mode were taken for the resultant spectra.

TEM studies

The samples for TEM analysis were prepared by ultracryomicrotomy with a Leica Ultracut UCT (Leica Mikrosystems GmbH, Vienna, Austria). Freshly sharpened glass knives with cutting edges of 45° were used to obtain cryosections of 50–70 nm thick. Because these samples were elastomeric in nature, the sample and glass knife temperatures during ultracryomicrotomy were kept constant at −110 and −120°C, respectively [these temperature were well below the glass-transition temperatures (T_gs) of SEBS]. The cryosections were collected individually in sucrose solu-

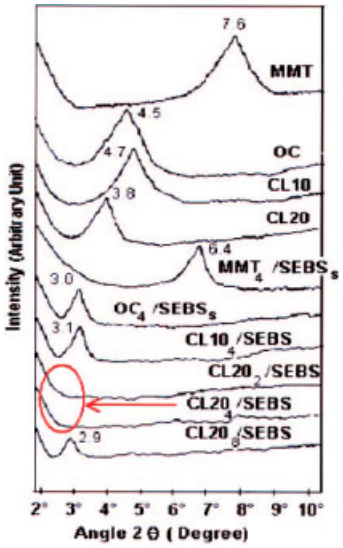

Figure 3 XRD spectra of the clays and SEBS–clay nanocomposites. [Color figure can be viewed in the online issue, which is available at www.interscience.wiley.com.]

tion and directly supported on a copper grid of 300 mesh in size. Microscopy was performed with a Philips (model no. CM 12, Philips Export BV, Eindhoven, The Netherlands) transmission electron microscope operating at an accelerating voltage of 120 kV.

AFM studies

The samples for AFM analysis were prepared by microtomy to cut out a fresh surface about 200 nm thick from the samples. The scanning and analysis of the samples were done using a multimode scanning probe microscope model with a Nanoscope IIIa controller by Digital Instruments, Inc. (Veeco Metrology Group, Santa Barbara, CA). The AFM measurements were carried out in air at ambient conditions (27°C) with tapping-mode probes with a constant amplitude. The scanning was done with a 125 μm long single-beam tapping-mode etched silicon probe, square pyramid in shape with a spring constant (k) of 20 N/m, nominal tip radius of curvature of 10 nm. Images were analyzed with Nanoscope IIIa image processing software. All images contained 256 data points. Both height and phase images with scan areas of 1.5 μ × 1.5 μ were analyzed.

Dynamic mechanical thermal analysis (DMTA)

DMTA of the nanocomposites along with the control SEBS were carried out with a DMTA IV (Rheometric Scientific, Inc., Piscataway, NJ) dynamic mechanical thermal analyzer. The sample specimens were analyzed in tensile mode at a constant frequency of 1 Hz, at 0.01% strain and within the temperature range of −80 to 80°C at a heating rate of 2°C/min. The data were analyzed by RSI Orchestrator application software (Rheometric Scientific, Inc.) on an ACER computer attached to the machine. Storage modulus (E'), loss modulus, and loss tangent (tan δ) were measured as a function of temperature for all the representative samples under identical conditions. The temperature corresponding to tan δ peak was taken as T_g.

Mechanical properties

Tensile specimens were punched out from the sheets (cast sheets for the solution process and molded thin sheets for the melt process) with ASTM Die-C. The tests were carried out as per the ASTM D 412-98 method in a universal tensile testing machine (Zwick 1445, Zwick GmbH and Co., Ulm, Germany) at a crosshead speed of 500 mm/min at 25 ± 2°C. The average of three results is reported.

RESULTS AND DISCUSSION

XRD analysis

The X-ray diffractograms of the modified and the unmodified clays are displayed in Figure 3. The corresponding 2θ values are reported in Table III. The peak 2θ value at 7.6° corresponding to d-spacing of 1.16 nm, appeared in the case of the unmodified MMT clay, whereas in the amine modified organophilic clays, the intergallery spacing increased, as shown in Table III, due to the impregnation of the amines and the hydrogenated tallow group into the gallery stacks. It was interesting that the increase in the gallery distance was also a function of the nature of the amines. The bulkier and more branched amines had larger intergallery spacing. These clays, intercalated and organophilic, permitted adequate space for polymer chains to enter into the clay galleries. For organically modified clays, OC, CL10, and CL20, the peak 2θ values were at 4.5,4.7, and 3.8°, corresponding to d-spacing of 1.96, 1.88, and 2.32 nm, respectively. The results of the

TABLE III
XRD Results of Clay and Clay–SEBS Nanocomposite Samples

Clay	2θ peak (°)	d-spacing (nm)
MMT	7.6	1.16
OC	4.5	1.96
CL10	4.7	1.88
CL20	3.8	2.32
MMT_4–SEBS	6.4	1.38
$CL20_2$–SEBS	—	—
$CL20_4$–SEBS	—	—
$CL20_8$–SEBS	2.9	3.04
$CL10_4$–SEBS	3.1	2.85
OC_4–SEBS	3.0	2.94

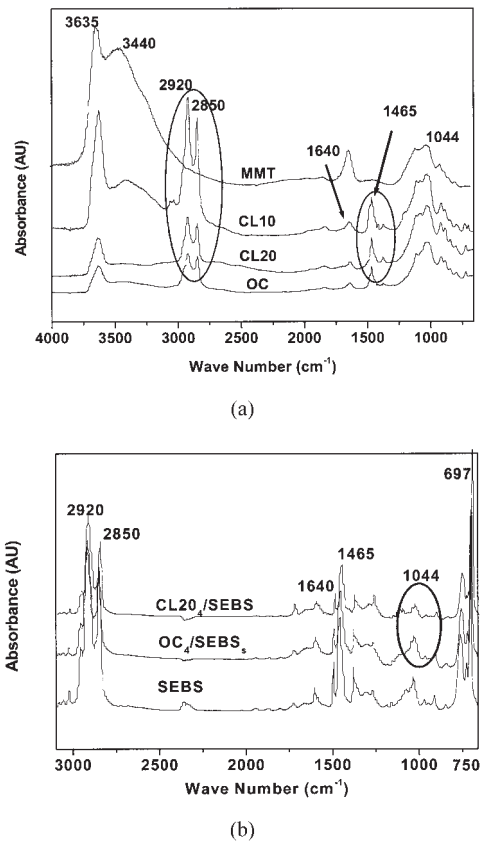

Figure 4 FTIR spectra of (a) unmodified and modified clays and (b) neat SEBS and its representative nanocomposites.

MMT and OC clays were in good agreement with those reported earlier from the same laboratory.[32–34]

The unmodified MMT clay galleries in the MMT_4–SEBS composites were expanded slightly by the SEBS chains, as evident from the peak at 6.4°. This peak corresponded to a gallery gap of 1.38 nm, which was larger than that of the MMT clay (1.16 nm). Intercalation could be inferred in the aforesaid system, imparting a 19% increase in gallery spacing. In the $CL20_4$–SEBS nanocomposites, no peak was observed, however, in either the solution or the melt intercalation process; this indicated extensive intercalation–exfoliation of the clay layers by SEBS. This inference was further strengthened by the morphological studies in the subsequent section. The $CL10_4$–SEBS and OC_4–SEBS composites, on the other hand, exhibited peaks at 3.1° and 3.0°, respectively. These peaks were observed at much lower angles and higher intergallery spacing of 2.85 and 2.94 nm, respectively, when the results were compared with those of the MMT clay. The plausible reason for better exfoliation of the clay layers might have been better interaction between the modified (hydrophobic in nature) nanoclay and the nonpolar polymer matrix. Moreover, the effect of steric factors caused by the bulky amines could not be ruled out.

The melt intercalation and solution-casting methods offered similar trends in peak shift and changes in gallery spacing.

The effect of the clay loading for CL20 was also investigated. CL20 at 2- and 4-phr doses in SEBS ($CL20_2$–SEBS, $CL20_4$–SEBS) showed exfoliation, whereas at the 8-phr dose ($CL20_8$–SEBS), there was a peak at 2.9° in the X-ray diffractogram. The latter gave an intergallery spacing of 3.04 nm, as given in Table III. The results indicate that there was a tendency toward agglomeration of the modified clay particles at higher loadings. The XRD results obtained for the aforesaid nanocomposites were in good agreement with the early works by Sadhu and Bhowmick[32–34] (for nitrile, styrene–butadiene, and polybutadiene rubber–clay nanocomposites), Vaia and Giannelis[50] (for PS nanocomposites), and Morgan and Gilman[51] (for cyanate esters, nylon 6, and polypropylene-*g*-maleic anhydride nanocomposites).

FTIR analysis

The results of the FTIR absorbance spectra for different clays and the SEBS–clay nanocopmposites are given in Figure 4(a) and 4(b), resepectively. The salient absorption peaks for the layered silicate clays and clay–SEBS nanocomposites are reported in Table IV.

The characteristic peaks for MMT clay were 3635 cm^{-1} due to O—H streching vibrations for the absorbed moisture and free OH groups, a broad band near 3440 cm^{-1} for intermolecular hydrogen bonded O—H, a sharp peak at 1640 cm^{-1} due to O—H bending, and a broad band near 1044 cm^{-1} for assymetric Si—O—Si streching frequency. On modification with hydrogenated tallow amines, the emergence of extra peaks at 2920, 2850, and 1465 cm^{-1} in the modified clays reflected the presence of the respective alkyl and amine groups in the system. The peaks at 2920 and 2850 cm^{-1} due to CH_2 streching overlapped with the

TABLE IV
Characteristic IR Absorption Peaks for Layered Silicate Clay and Clay–SEBS Nanocomposites

Characteristic peak value (cm^{-1})	Peak assignment
3635	O—H streching
Broad band near 3440	Intermolecular hydrogen bonded O—H
2920	CH_2 streching
2850	NC—H and CH_3 streching
1640	O—H bending
1465	Assymetric deformation peak of CH_3 and CH_2 and N—H deformation bending
1044	Asymetric Si—O—Si streching
697	Styrenic C—H streching

N—C—H streching peaks. Therefore, the segregation of these peaks could not be precisely done from the spectra. The broad band at 3440 cm^{-1} was diminished in the modified clays, mainly because of imparted hydrphobicity or, in other terms, increased organophilicity generated in the systems due to the modification by hydrocarbon chain (tallow) amines. The peak height at 1640 cm^{-1} decreased considerably in the amine-modified clays compared to that in sodium MMT, mostly because of the hydrophobicity generated in the modified clays. The appearance of a strong peak at 1465 cm^{-1} supported the presence of amine–hydrocarbon chains in the modified clays (N—H deformation–bending peak).

The FTIR spectra of the SEBS–clay nanocomposite [Fig. 4(b)] revealed the appearance of the clay peaks (viz. 2920, 2850, 1640, 1465, and 1044 cm^{-1}) in MMT_4–SEBS and $CL20_4$–SEBS with the hydrocarbon peaks (viz. 2920 and 2850 cm^{-1}) due to the SEBS matrix. A very sharp peak at 697 cm^{-1} appeared for all of the nanocomposites due to the styrene moiety present in SEBS. Although apparently FTIR study did not alone provide any major conclusions regarding the charateristics of the nanocomposites, this study verified the incorporation of the modifying agent into the structure of the clay and polymer–clay interactions.

Morphological study

TEM analysis

The TEM image of MMT_4–SEBS in Figure 5(a) demonstrated the existence of clay agreegates within the SEBS matrix. This might have been due to the poor interaction between the MMT and the SEBS matrix. The XRD peak at 6.4° for this system showed agglomeration. TEM images of the representative nanocomposites $CL20_4$–$SEBS_s$ [where the subscript *s* indicates that SEBS was cast in the solution process; Fig. 5(b)] and OC_4–$SEBS_s$ [Fig. 5(c)] displayed the presence of both intercalated and exfoliated moprphologies of the clay layers within the SEBS matrix. In OC_4–$SEBS_s$, a quasidiscrete layer formation of the clay was obtained, whereas $CL20_4$–$SEBS_s$ furnished an exfoliated morphology of the nanoclay dispersed in the SEBS matrix, which was further elucidated by the AFM studies reported in the next section. This kind of morphology in the nanocomposites was anticipated on account of the better compatibilization between the modified nanoclay and SEBS. The resultant exfoliated stacks of CL20 in the SEBS system were 10–20 nm thick on average, which however, was not detected in the X-ray diffractograms if they were exfoliated in an ordered fashion. These stacks were further separated by an average distance of 100–110 nm in the micrographs shown in Figure 5(b). On the other hand, for the OC_4–$SEBS_s$ system, the average intercalated–exfoliated particle size was in the range 35–40 nm, but occasionally, these were associated with agglomerated portions. With the same procedure, earlier workers reported the exfoliation of OC in styrene–butadiene, polybutadiene, and nitrile and butyl rubbers.[32–34]

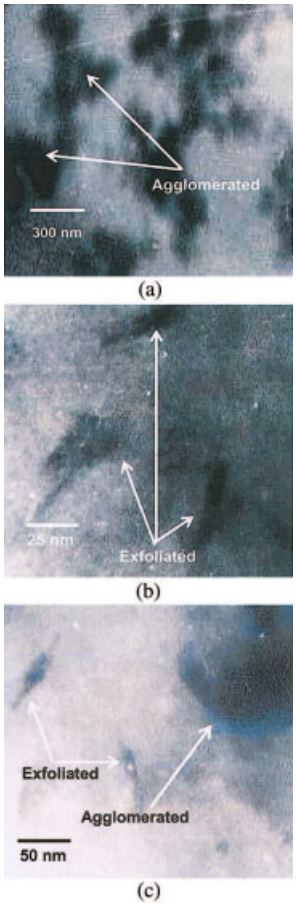

Figure 5 TEM pictures of (a) MMT_4–$SEBS_s$, (b) $CL20_4$–$SEBS_s$, and (c) OC_4–$SEBS_s$. [Color figure can be viewed in the online issue, which is available at www.interscience.wiley.com.]

AFM analysis

AFM was used to investigate the nanomorphology and properties of the neat block copolymer and SEBS and its clay nanocomposites. AFM study of the SEBS–clay nanocomposites (Fig. 6) furnished interesting observations. The tapping mode was employed to analyze the attributes of the lamellar phase characteristics in different processes of nanocomposite preparation, differences in the topographical features in the presence and absence of dispersed nanofillers. Height and phase imaging revealed distinctly different bulk morphologies of the nanocomposites prepared in the melt and solution processes, as shown in Figure 6(a,b). In solvents, the hydrodynamic volume of the polymer chain was larger than that of the neat polymer, which

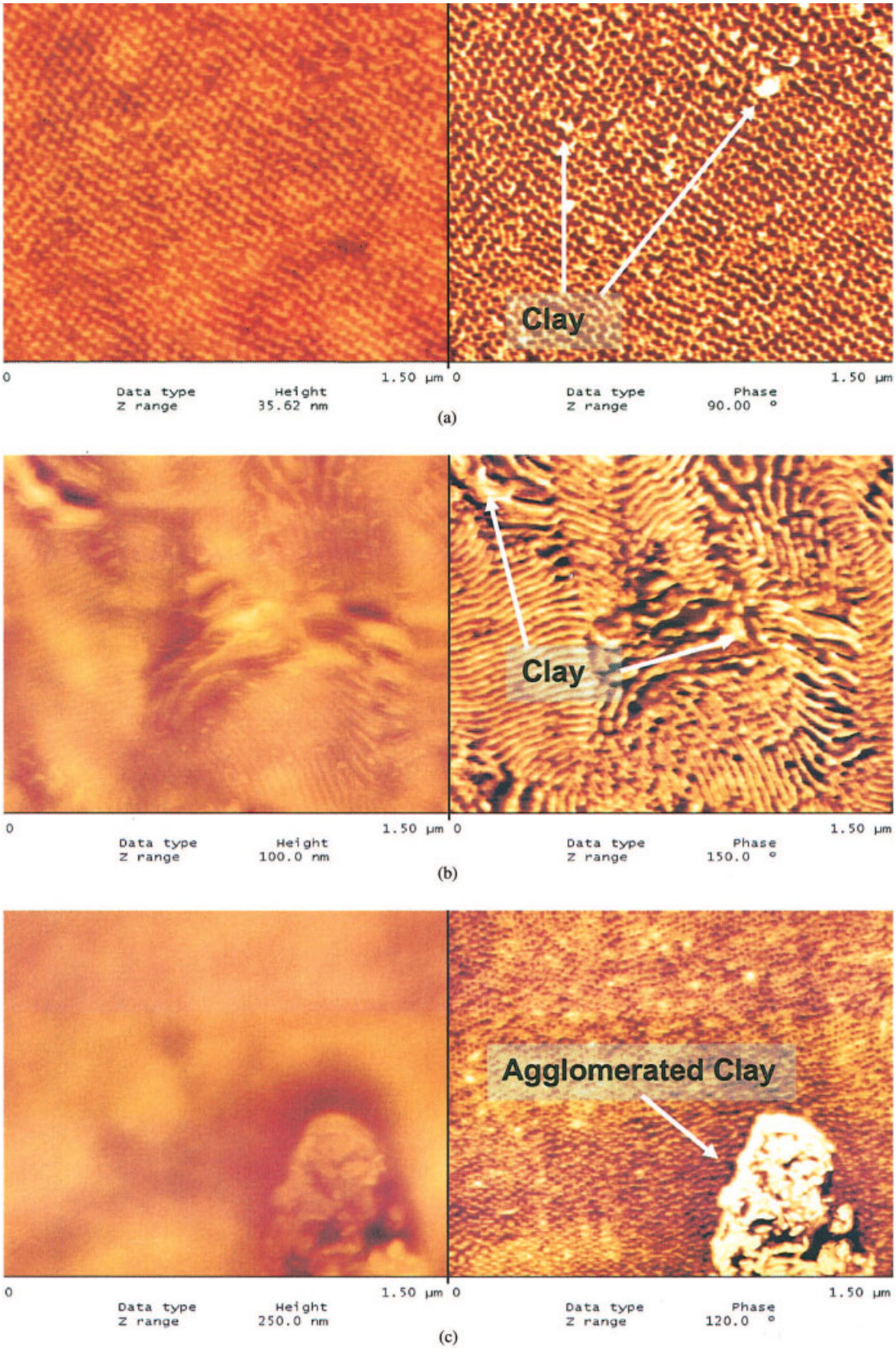

Figure 6 Height and phase AFM images of the bulk of nanocomposites: (a) $CL20_4$–$SEBS_m$, (b) $CL20_4$–$SEBS_s$, and (c) composite MMT_4–$SEBS_s$. [Color figure can be viewed in the online issue, which is available at www.interscience.wiley.com.]

furnished a lamellar morphology, whereas a regular array-like structure was obtained in the melt nanocomposites. The hard styrenic phases of SEBS were the brighter portion in the topographical representation [Fig. 6(a)]. In the block copolymeric morphology, the typical lamellar dimension of the block copolymer was in the range 25–30 nm. AFM analysis revealed that the bright white clay layers in the $CL20_4$–SEBS nanocomposite were distributed in the lamellar phases as evident from Figure 6(a,b). The modified clays exhibited high-structured finer particles 70–90 nm in length and 10–12 nm in width. There was an indication of good dispersion of the modified CL20 clays in the SEBS matrix as seen earlier in the transmission electron micrographs [Fig. 5(b)]. The best exfoliation demonstrated by $CL20_4$ in the SEBS system indicated the importance of the intercation between the clay and the polymer in the nanocomposites (PSLNCs).

As shown in Figure 6(c), agglomerated structures with an average size of approximately 700 nm were observed in the MMT_4–SEBS system. Although the interlayer distance of the anisotropic silicates increased only 19% with respect to the copolymer due to a slight intercalation of the copolymer chains into the clay interlayers in the MMT_4–SEBS composites, the presence of agglomeration was still confirmed from the AFM and TEM studies [Fig. 5(a)] and the appearance of the XRD peaks (Fig. 3), as discussed in the preceding sections.

DMTA

Figure 7(a–c) shows the dynamic mechanical analysis of the hybrid nanocomposites within the temperature range −80 to 80°C. The dynamic storage modulus (E') in Figure 7(a) elucidates the effect of the clays on the SEBS system. $CL20_4$–$SEBS_s$ showed a markedly improved dynamic E' in both the glassy and the rubbery region compared to the control SEBS. This was possibly due to the better polymer–organically modified clay interaction, as already mentioned. However, the OC_4–$SEBS_s$ nanocomposite did not exhibit as much improvement as $CL20_4$–$SEBS_s$ or $CL20_4$–$SEBS_m$ (where the subscript m indicates that SEBS was molded after extrusion). The E' values of OC_4–$SEBS_s$ were marginally higher than that of the control, especially in the rubbery region. The unmodified clay filled composite MMT_4–$SEBS_s$ possessed a lower modulus than the control in the rubbery region.

Comparative plots of tan δ against temperature, which ranges from −80 to 80°C, for all of the nanocomposites along with the unfilled neat SEBS are presented in Figure 7(b). With SEBS being a triblock copolymer, two distinct T_gs, one at −60°C for the rubber phase and another at 65°C for the plastic phase, were obtained for both neat SEBS and its nanocomposites.

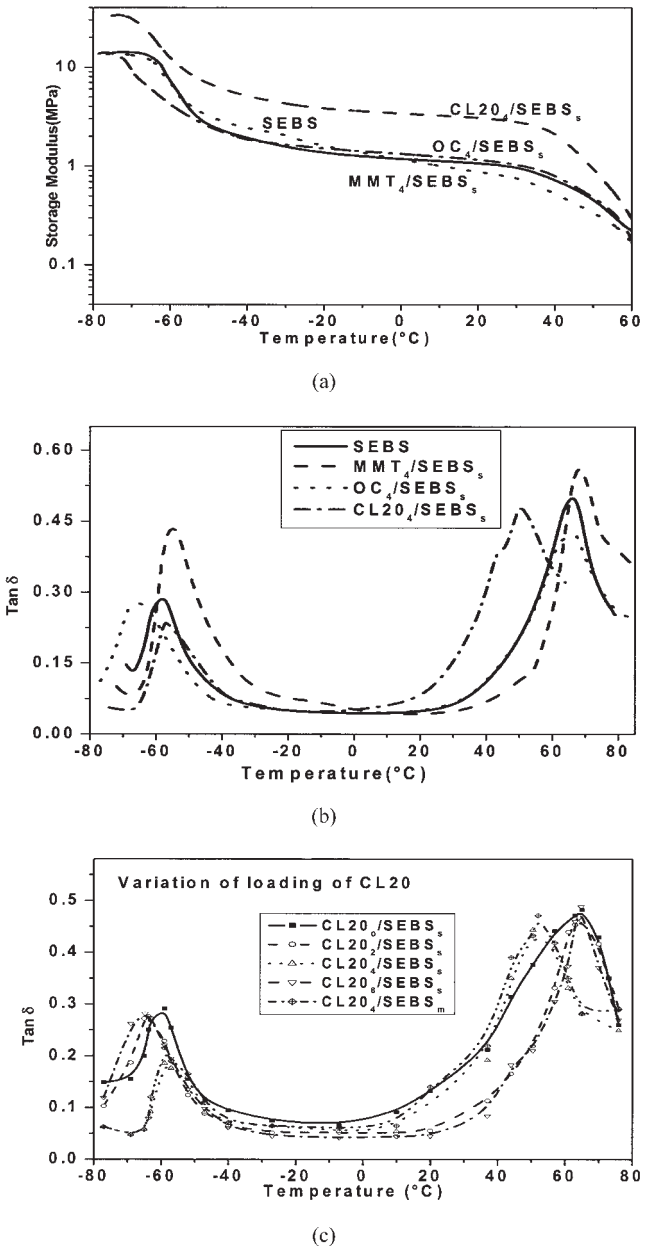

Figure 7 (a) Plot of log E' versus temperature, (b) tan δ versus temperature plots for SEBS and the clay–SEBS nanocomposites, and (c) variation of tan δ for different doses of CL20 in nanocomposites prepared through the solution and melt processes.

For MMT_4–$SEBS_s$, both the peak heights (for the elastomeric and the plastic phases) increased, which kept the peak position almost the same. This might have been due to the agglomeration effect of MMT clays within the TPE matrix and also its influence in the disruption of the orderly structures of SEBS. This was in line with the TEM and AFM observations. On the other hand, in the OC_4–$SEBS_s$ system, there was a change in the plastic T_g height with no change in the peak position, and the T_g of the rubber phase shifted by −5°C, which indicated marginal plasticization by

TABLE V
T_g and tan δ Values for SEBS and the Composites with SEBS and Variation with CL20 Dose in the Nanocomposites

Sample	T_{g1} (°C)	tan δ_1	T_{g2} (°C)	tan δ_2
SEBS	−57.8	0.29	66.0	0.48
MMT_4–SEBS	−57.6	0.48	69.1	0.59
OC_4–SEBS	−62.8	0.28	66.8	0.50
$CL20_0$–$SEBS_s$	−58.0	0.29	66.0	0.48
$CL20_2$–$SEBS_s$	−60.0	0.27	65.0	0.47
$CL20_4$–$SEBS_s$	−57.1	0.19	50.5	0.45
$CL20_0$–$SEBS_s$	−61.0	0.28	64.8	0.48
$CL20_4$–$SEBS_m$	−57.5	0.21	52.1	0.47

T_{g1} = glass-transition temperature of the elastic phase of the system; tan δ_1 = highest loss tangent corresponding to T_{g1}; T_{g2} = glass-transition temperature of the plastic phase of the system; tan δ_2 = highest loss tangent corresponding to T_{g2}.

the C18 hydrocarbon chains of the modifier amine. $CL20_4$–$SEBS_s$ provided an interesting observation. The tan δ peak height of the rubber phase was reduced by 35% compared to that of the neat SEBS, whereas the tan δ peak of the plastic region shifted towards the rubbery phase by 26% [from 66 to 51°C, as shown in Fig. 7(b–c)]; the corresponding results are reported in Table V. These results are possibly due to interaction of CL20 with both phases of SEBS in the bulk, which corroborates our earlier AFM observations. The OC_4-filled composites exhibited a small peak at 3.0° in the XRD diagram, whereas the peak disaappeared in the $CL20_4$ nanocomposite. Dynamic mechanical analysis elucidated that CL20 gave by far the best results compared to the MMT–clay composite or the OC-modified nanocomposite due to relatively better polymer–organoclay compatibilty and also due to exfoliation and better dispersion.

The tan δ of the samples containing different doses of CL20 in SEBS [Fig. 7(c)] illustrated that the peak was reduced and shifted with respect to the control SEBS. The 2 phr loading of CL20 in SEBS did not show any significant change in the peak height and the peak position of both the plastic and the rubber phases compared to the neat SEBS. Similar to the effect in OC_4–$SEBS_s$, the 8-phr loading in $CL20_8$–$SEBS_s$ showed a shift of the rubbery phase by −5°C from the control SEBS, mainly because of the plasticization effect of the hydrocarbon chains of the nanoclay. However, it showed no change in the peak height in the plastic phase. The lowest tan δ was observed both in the rubbery and the plastic phases for the 4-phr CL20–SEBS sample compared to its 0-, 2-, and 8-phr loadings [Fig. 7(c)]. This may have been due to the better dispersion and interaction of the nanoclay at the 4-phr level. A dilution effect was observed with higher loadings (8 phr) of CL20 nanoclay in the SEBS matrix. CL20 with the same 4-phr loading in the melt process ($CL20_4$–$SEBS_m$) showed a similar shift of tan δ peaks as that of $CL20_4$–$SEBS_s$. In the melt process, the tan δ peak increased somewhat compared to that in the solution process, which may have been due to a higher probability of polymer–nanoclay intercalation in the solvent-swollen conditions in the solution process.

Analysis of the mechanical properties

Representative tensile stress–strain curves for the SEBS–clay nanocomposites along with the control SEBS are shown in Figure 8(a–c), which depicts the variation of clay structure and clay loading. The behavior of the nanocomposites prepared in the solution and the melt processes is reported also in Table VI. The difference between the amines was probably in the extent of intercalation–exfoliation. The stress–strain curves indicated typical behavior of an elastomer: the stress increased with strain abruptly after 200% strain. The addition of a small amount of clay did not change the typical nature of the curves [Fig. 8(a)]. Because the extent of reinforcement was a function of the polymer–filler interaction, the nanocomposites showed a higher modulus, ultimate stress, and work to break over the control and the unmodified

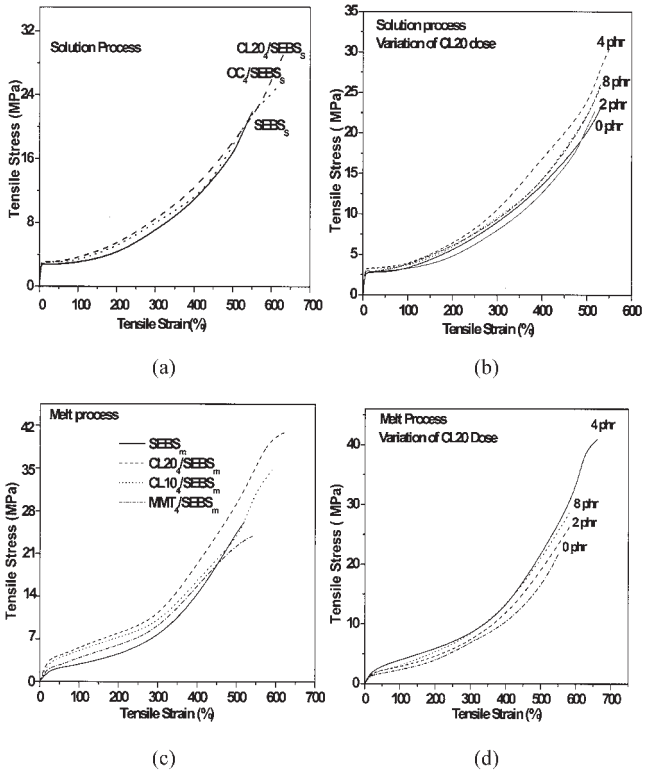

Figure 8 Tensile stress–strain plots of the SEBS–clay nanocomposites: effects of (a) the modified clays on SEBS in the solution process, (b) variation of CL20 dose in the solution process, (c) the unmodified and the modified clays on SEBS properties in the melt process, and (d) variation CL20 dose in the melt process on SEBS.

TABLE VI
Mechanical Properties of SEBS and Its Clay Nanocomposites

Sample	Modulus (MPa) 50%	Modulus (MPa) 300%	Tensile strength (MPa)	Elongation at break (%)	Work to break (kJ/m^2)
$SEBS_s$	2.6	7.0	23.8	520	19.2
$SEBS_m$	1.9	7.0	22.5	530	20.1
MMT_4–$SEBS_m$	2.2	8.2	24.2	550	22.1
$CL20_2$–$SEBS_m$	2.4	7.5	25.8	590	27.8
$CL20_4$–$SEBS_m$	3.2	10.0	40.9[a]	660[a]	38.3[a]
$CL20_8$–$SEBS_m$	2.4	9.0	29.1	600	32.6
$CL10_2$–$SEBS_s$	2.6	9.5	22.0	500	19.0
$CL10_4$–$SEBS_s$	3.2	9.5	23.5	520	20.1
$CL10_8$–$SEBS_s$	2.7	8.5	27.2	560	24.9
$CL20_2$–$SEBS_s$	2.6	8.4	24.0	540	22.8
$CL20_4$–$SEBS_s$	3.5[a]	11.0[a]	31.6	580	29.2
$CL20_8$–$SEBS_s$	3.2	9.5	27.2	560	23.9
OC_4–$SEBS_s$	3.4	8.8	26.9	630	29.2

[a] Highest value.

clay loaded SEBS composites depending on the structure of the clay.

Figure 8(b) reveals the stress–strain curve of SEBS filled with 2–8 parts of the modified nanoclay. The curve of 4-phr CL20 was above all of the other curves, and this 4-phr loading of CL20 in the melt process imparted the highest physical properties, beyond which these tended to decline, possibly due to slight agglomeration, as evidenced from the XRD peak at 2.9° for the $CL20_8$–SEBS system. Similar results were been reported from our laboratory on styrene–butadiene rubber with different styrene contents and nitrile rubber with different nitrile contents.[32–34] It was also reported that the optimized filler loading is influenced by the nature of rubber. The samples made by solution process also showed optimized properties at a 4-phr loading of the modified nanoclay.

As shown in Table VI, for $CL20_4$–$SEBS_m$, there were increments of 82, 43, and 91% in tensile strength (TS), modulus, and work to break, respectively, compared to the neat SEBS system. The higher polymer–filler interaction was a result of exfoliation–intercalation in the case of the modified nanoclay. These values were much higher than those of the MMT clay–SEBS (MMT_4–$SEBS_m$) samples (8, 17, and 10% increments compared to neat SEBS).

In the solution process, although OC_4–$SEBS_S$ showed an increase in modulus of 30% and in TS by 13%, the improvements were far more pronounced in $CL20_4$–$SEBS_s$ (57 and 33% in modulus and TS, respectively). Among the samples with 2-, 4-, and 8-phr loadings of CL20, the 4-phr loading showed the maximum improvement in the aforesaid properties [Fig. 8(b)].

The increase in TS was about 82% in $CL20_4$–$SEBS_m$ with respect to the control $SEBS_m$. As TS depended on rubber–filler interaction, TS and elongation at break increased with filler loading up to 4 phr but decreased progressively with increasing levels of CL20 loading up to 8 phr [Table VI and Figs. 8(d) and 9]. This dilution effect may have been due to agglomeration at the higher filler loading (8 phr), which was supported by the XRD results and DMTA study.

Another nanoclay, CL10, was used to understand the behavior of nanoclay on the mechanical properties. Although CL10 nanoparticles imparted improved properties over the control and the unmodified clay filled composites, the extent of improvement was slightly lower than that of the CL20–SEBS nanocomposites [Fig. 8(c) and Table VI].

The mechanical properties of the nanocomposite samples prepared by solution and melt intercalation processes are compared in Figure 9. The difference between these two systems may have been due to the

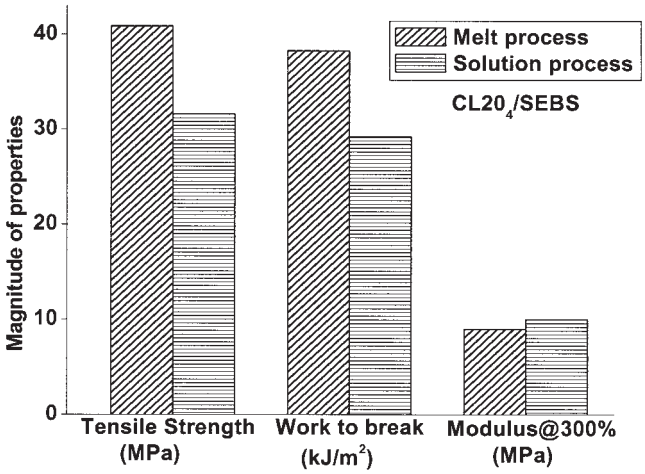

Figure 9 Comparative plots of the mechanical properties achieved for $CL20_4$–SEBS systems in the melt and solution processes.

difference in morphology, as revealed by AFM studies. In both the cases, the 4-phr loading of CL20 produced exfoliation. Although the maximum tensile stress, elongation at break, and work to break were higher (TS by 26% and work to break by 32%) for the samples prepared with the melt intercalation technique ($CL20_4$–$SEBS_m$) compared to that prepared in solution process ($CL20_4$–$SEBS_s$), the 50 and 300% moduli were higher for the PLSNC prepared in the solution process (Table VI and Fig. 9). The initial sharp increase in modulus within the Hookean region was more prominent in the solution-cast samples [Fig. 8(a–d)]. This possibly was the effect of the distinct morphological differences and location of the nanoparticles, as evident from the AFM studies.

CONCLUSIONS

1. SEBS nanocomposites were prepared by solution and melt blending processes with different types of nanoclays, such as CL10 and CL20, tallow amine modified clays, and OC, an organically modified MMT clay prepared in the laboratory with octadecyl amine (C18) chloride by a cation-exchange reaction. The loading of nanoclays in SEBS system was varied. The clays and the nanocomposites were characterized by XRD, FTIR spectroscopy, TEM, and AFM. The mechanical and dynamic mechanical properties of the nanocomposites were investigated.
2. X-ray diffractograms indicated expansions of the clay gallery with the incorporation of amines. The X-ray diffractograms did not show any 2θ peak between 3 and 10° for the $CL20_2$–SEBS and $CL20_4$–SEBS nanocomposites, which indicated exfoliation, whereas $CL20_8$–SEBS and OC_4–SEBS showed intercalated structures, as evidenced from small peaks at 2.9 and 3.0°, respectively. MMT_4–SEBS exhibited agglomeration, which indicated the formation of microcomposites.
3. The morphological studies by AFM and TEM revealed exfoliation in the case of CL20 and agglomeration in the unmodified MMT-clay-filled SEBS composites at 4-phr loading. The location of the clay was indicated clearly in the micrographs.
4. A comparison was made for the first time (between the solution and melt intercalation techniques) as far as TPE was concerned. AFM studies showed distinct differences in the solution and melt morphologies for the modified nanoclay–SEBS systems.
5. $CL20_4$–SEBS showed a much improved dynamic storage modulus (E') compared to the control SEBS, OC_4- and MMT_4-filled composites. The lowest tan δ was observed for the 4-phr CL20–SEBS sample, as compared to 0-, 2-, and 8-phr loadings. A dilution effect was observed with the higher loading (8 phr) of the CL20 nanoclay in the SEBS matrix. CL20 with the same 4-phr loading in the melt process ($CL20_4$–$SEBS_m$) showed a similar shift of tan δ peaks as that of $CL20_4$–$SEBS_s$.
6. CL20-filled SEBS nanocomposites displayed superior moduli and tensile properties in the melt intercalation and solution processes compared to OC-, CL10-, and MMT-filled SEBS composites. CL20 (4 parts) in SEBS, both in the solution and melt processes, gave the best mechanical results. The direct melt intercalation process further conferred better results with respect to TS and toughness compared to the solution process, although the latter rendered improvements in 50 and 300% moduli compared to the former.

References

1. (a) Pinnavaia, T. J.; Beall, G. W. Polymer–Clay Nanocomposites; John Wiley & Sons Ltd.: Chichester, England, 2001. (b) Krishnamoorti, R.; Vaia, R. A. Polymer Nanocomposites: Synthesis, Characterization, and Modeling; Washington, DC: American Chemical Society, 2001.
2. Roy, S. S.; Okamoto, M. Prog Polym Sci 2003, 28, 1539.
3. BCC Research Site. http://www.bccresearch.com/editors/rp-234r.html (accessed Mar 2004).
4. Theng, B. K. G. Formation and Properties of Clay–Polymer Complexes; Elsevier: New York, 1979; Vol. 9.
5. Silvia, A. S.; Mitchell, C. A.; Tse, M. F.; Wang, H. C.; Krishnamoorti, R. J Chem Phys 2001, 115, 15.
6. Lee, J. Y.; Lee, H. K. Mater Chem Phys 2004, 85, 410.
7. Akinobu, S.; White, J. L. J Appl Polym Sci 2004, 91, 1951.
8. Kojima, Y.; Usuki, A.; Kawasumi, M.; Okada, A.; Kurauchi, T.; Kamigaito, O. J Polym Sci Part A: Polym Chem 1993, 31, 983.
9. Kojima, Y.; Usuki, A.; Kawasumi, M.; Fukushima, Y.; Okada, A.; Kurauchi, T.; Kamigaito, O. J Mater Res 1993, 8, 1185.
10. Kojima, Y.; Usuki, A.; Kawasumi, M.; Fukushima, Y.; Okada, A.; Kurauchi, T.; Kamigaito, O. J Mater Res 1993, 8, 1775.
11. Gilman, J. W.; Jackson, C. L.; Morgan, A. B.; Harris, R.; Manias, E.; Giannels, E.; Wuthenow, M.; Hilton, D.; Phillips, S. H. Chem Matter 2000, 12, 1866.
12. Lepoittevin, B.; Devalckenaere, M.; Pantoustier, N.; Alexandre, M.; Kubies, D.; Calberg, C.; Jerome, R.; Henrist, C.; Cloots, R.; Dubois, P. Polymer 2002, 43, 4017.
13. Usuki, A.; Koiwai, A.; Kojima, Y.; Kawasumi, M.; Okada, A.; Kurauchi, T.; Kamigaito, O. J Appl Polym Sci 1995, 55, 119.
14. Shelley, J. S.; Mather, P. T.; Devries, K. L. Polymer 2001, 42, 5849.
15. Agag, T.; Takeichi, T. Polymer 2001, 42, 3399.
16. Lincon, D. M.; Vaia, R. A.; Wang, Z. G.; Hsiao, B. S. Polymer 2001, 42, 1621.
17. Kim, G. M.; Lee, D. H.; Hoffmann, B.; Kressler, J.; Stoppelmann, G. Polymer 2001, 42, 1095.
18. Rayneud, E.; Jouen, T.; Ganthier, C.; Vigier, G.; Varlet, J. Polymer 2001, 42, 8759.
19. Kawasumi, M.; Hasegawa, N.; Kato, M.; Usuki, A.; Okada, A. Macromolecules 1997, 30, 6333.
20. Ma, J.; Qi, Z.; Hu, Y. J Appl Polym Sci 2001, 82, 3611.
21. Manias, E.; Touny, A.; Wu, L.; Strawhecker, K.; Lu, B.; Chung, T. C. Chem Matter 2001, 13, 3516.
22. Zanetti, M.; Camino, G.; Reichert, P.; Mulhaupt, R. Macromol Rapid Commun 2001, 22, 176.

23. Park, C. I.; Park, O. O.; Lim, J. G.; Kim, H. J. Polymer 2001, 42, 7465.
24. Fu, X.; Qutubuddin, S. Polymer 2001, 42, 807.
25. Zongneng, Q.; Yongmei, M.; Zhang, Z.; Qun, Y. Huagong Jinzhan 2001, 20, 2.
26. Vaia, A. R.; Sauer, B. R.; Tse, O. K.; Giannelis, E. P. J Polym Sci 1997, 35, 59.
27. Strawhecker, K. E.; Manias, E. Chem Matter 2000, 12, 2943.
28. Kornman, X. Synthesis and Characterisation of Thermoset–Clay Nanocomposites; Division of Polymer Engineering, Lulea University of Technology: Lulea, Sweden.
29. Ray, S.; Bhowmick, A. K. Rubber Chem Technol 2001, 74, 835.
30. Pramanik, M.; Srivastava, S. K.; Samantaray, B. K.; Bhowmick, A. K. J Polym Sci Part B: Polym Phys 2002, 40, 2065.
31. Vu, Y. T.; Mark, J. E.; Pham, L. H.; Engelhardt, M. J Polym Sci 2001, 82, 1391, and references therein.
32. Sadhu, S.; Bhowmick, A. K. J Polym Sci Part B: Polym Phys 2004, 42, 1573.
33. Sadhu, S.; Bhowmick, A. K. J Appl Polym Sci 2004, 92, 698.
34. Sadhu, S.; Bhowmick, A. K. Rubber Chem Technol 2003, 76, 860.
35. Ma, J.; Zhang, S.; Qi, Z. J Appl Polym Sci 2001, 82, 1444.
36. Pramanik, M.; Srivastava, S. K.; Samantaray, B. K.; Bhowmick, A. K. J Appl Polym Sci 2003, 87, 2216.
37. Zanetti, M.; Camino, G.; Thomann, R.; Mulhaupt, R. Polymer 2001, 42, 4501.
38. Cho, J. W.; Paul, D. R. Polymer 2001, 42, 1083.
39. Fornes, T. D.; Yoon, P. J.; Keskkula, H.; Paul, D. R. Polymer 2001, 42, 9929.
40. Vaia, R. A.; Giannelis, E. P. Macromolecules 1997, 30, 7990.
41. Vaia, R. A.; Ishii, H.; Giannelis, E. P. Chem Mater 1993, 5, 1694.
42. Juma, N. G. The Pedosphere and Its Dynamic: Mineralogy, Clay Crystals; 1998.
43. Tjong, S. C.; Meng, Y. Z. J Polym Sci Part B: Polym Phys 2003, 41, 2332.
44. Chen, Z.; Gong, K. J Appl Polym Sci 2002, 84, 1499.
45. Laus, M.; Francescangeli, O.; Sandrolini, F. J. Mater Res 1997, 12, 3134.
46. Liao, M.; Zhu, J.; Xu, H.; Li, Y.; Shan, W. J Appl Polym Sci 2004, 92, 3430.
47. Tety, K.; Mauritz, K. A. Polym Prepr (Am Chem Soc Div Polym Chem) 2003, 44, 1106.
48. Mauritz, K. A.; Blackwell, R. I.; Beyer, F. L. Polymer 2004, 45, 3001.
49. Mauritz, K. A.; Storey, R. F.; Reuschle, D. A.; Beck Tan, N. Polymer 2002, 43, 5949.
50. Vaia, R. A.; Giannelis, E. P. Macromolecules 1997, 30, 8000.
51. Morgan, A. B.; Gilman, J. W. J Appl Polym Sci 2003, 87, 1329.